Materials & Design 216 (2022) 110538

Contents lists available at ScienceDirect

Materials & Design

journal homepage: www.elsevier.com/locate/matdes

Standard mechanical testing is inadequate for the mechanical characterisation of shape-memory alloys: Source of errors and a new corrective approach

Sofia Di Leonardo [a,b,c], Giuseppe Pitarresi [b], Gaetano Burriesci [a,c,*]

[a] Bioengineering Group, Ri.MED Foundation, Palermo, Italy
[b] Engineering Department, University of Palermo, Italy
[c] UCL Cardiovascular Engineering Laboratory, University College London, UK

HIGHLIGHTS

- Uniaxial tension tests on nitinol plates strongly depart from the uniaxial idealisation.
- Results from tension test on nitinol plates can be affected by major inaccuracy.
- DIC technique can help to ensure the reliability of tension tests.
- Geometrical explanation of Lüders bands formation.

GRAPHICAL ABSTRACT

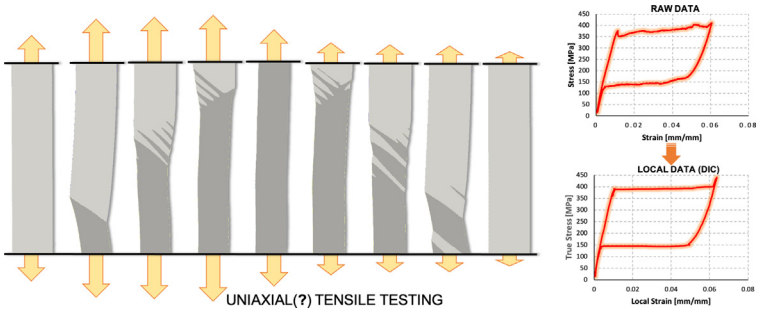

ARTICLE INFO

Article history:
Received 16 December 2021
Revised 5 March 2022
Accepted 6 March 2022
Available online 09 March 2022

Keywords:
Shape memory alloy (SMA)
Uniaxial tension test
Local mechanical behaviour
Digital image correlation (DIC)

ABSTRACT

Thanks to its unique behaviour characterised by a superelastic response, Nitinol has now become the material of preference in a number of critical applications, especially in the area of medical implants. However, the reversible phase transformation producing its exceptional comportment is also responsible for a number of phenomena that make its mechanical characterisation particularly complex, by hindering the assumptions at the very basis of common uniaxial tensile testing. This necessarily reduces the level of safety and design optimization of current applications, which rely on incorrect mechanical parameters. In this study, the spurious effects introduced by the unconventional material behaviour during uniaxial tensile testing are analysed by means of digital image correlation (DIC), identifying the onset of undesirable material inhomogeneities and bending moments that are dependent on the test setup and strongly limit the reliability of standard characterisation. Hence, a more accurate and systematic testing approach, exploiting the ability of DIC to analyse the local mechanical response at specific regions of the test specimen, is presented and discussed.

© 2022 Published by Elsevier Ltd. This is an open access article under the CC BY-NC-ND license (http://creativecommons.org/licenses/by-nc-nd/4.0/).

1. Introduction

Nitinol is an equiatomic Ni-Ti alloy characterised by the ability to recover levels of strain orders of magnitude larger than standard metals (commonly indicated as super-elasticity or super-elastic behaviour) and exert more stable forces for a range of deformations. Thanks to these unique properties this material is increas-

* Corresponding author at: Room 507A, Malet Place Engineering Building, Torrington Place, London WC1E 7JE, UK.
E-mail address: g.burriesci@ucl.ac.uk (G. Burriesci).

https://doi.org/10.1016/j.matdes.2022.110538
0264-1275/© 2022 Published by Elsevier Ltd.
This is an open access article under the CC BY-NC-ND license (http://creativecommons.org/licenses/by-nc-nd/4.0/).

Nomenclature

E_A	Young's modulus of the austenitic phase;
E_M	Young's modulus of the martensitic phase;
v_A	Poisson's ratio of the austenitic phase;
v_M	Poisson's ratio of the martensitic phase;
σ_s^{AM}	initial stress for the austenite to martensite phase transformation;
σ_f^{AM}	final stress for the austenite to martensite transformation;
σ_{UPS}	upper plateau strength (at 3% of strain during loading);
σ_s^{MA}	initial stress for the martensite to austenite phase transformation;
σ_f^{MA}	final stress for the martensite to austenite phase transformation;
σ_{LPS}	lower plateau strength (at 2.5% of strain during);
σ_E	reference stress for young modulus calculation (Eq. (1))
ε_L-	transformation strain (axial) associated with the austenite to martensite transformation
$\varepsilon_{Lx}-$	trasversal transformation strain associated with the austenite to martensite transformation
v_T	Poisson's ratio associated with the transformation.

ingly used in in the automotive, aerospace and automation industry [1–3], and its biocompatibility has contributed to make it establish as a material of preference in a number of medical devices including cardiovascular, orthopaedic and orthodontic implants [4].

The criticality of these applications, which demands the highest level of safety and design optimisation, requires the accurate characterisation of the material mechanical behaviour at the working temperatures. This is normally achieved by means of uniaxial tension testing, as accepted by regulatory standards such as the ASTM E8 [5], which describes the methods for tension testing of homogeneous and isotropic metals. In the case of the assessment of superelastic Ni-Ti alloy, this is integrated by the ASTM F2516 [6], which provides additional details for the extraction of the upper and lower plateau strength and residual elongation from the test data.

Although these tests are based on the idealised assumption of homogeneity, previous studies have observed that when the super-elastic behaviour is exhibited during the test, specimens comprise regions with different crystal structures and mechanical properties. In fact, the material superelastic behaviour is the result of a stress-induced phase transformation from austenite to martensite, which initiates at localised Lüders bands [7,8]. These regions, characterised by very large strains of the order of 6–8% [9] (or larger, in the case of other SMA systems, such as Fe and Cu-based alloys [10–11]), progressively expand with the specimen elongation, until the entire gauge length has transformed. This invalidates the assumption of homogeneity of the test material, potentially reducing the reliability of the information obtained from standard tension testing.

As a consequence, test results commonly used to characterise Nitinol need to be reinterpreted to determine if and how they can still provide quantitative parameters suitable to describe the mechanical behaviour of the material. This work presents an analysis of the phenomena occurring in a Nitinol plate specimen during quasistatic uniaxial tension testing in the super-elastic region, by means of digital image correlation (DIC). The study examines the limitations introduced by the presence of inhomogeneous regions varying in extension during the test. This analysis is then used to implement a new approach to extract more objective parameters from the standard uniaxial test, providing a more accurate mechanical characterisation of superelastic Ni-Ti alloys.

2. Materials and methods

A test specimen was obtained from a Nitinol plate (0.2 mm thick, 6.35 mm large and 35 mm high) of transformation temperature equal to 13 °C, as determined from differential scanning calorimetry analysis [12]. A black random speckle was applied with an airbrush on one side of the plate specimen, previously painted white (the specimen surface is shown in Fig. 1). The sample was tested on a uniaxial electromechanical testing machine Instron 3367, at room temperature (20 °C). Displacement was applied through a sequence of quasi-static triangular waves, at a cross-head speed of 0.5 mm/min. Progressively increasing peaks of deformation, raising of 1% at each cycle, were applied, monitoring the stress–strain diagram in order to arrest the applied deformation at the lowest percentage integer ensuring that the stress-induced martensitic transformation for the whole gauge length was achieved (i.e. the upper transformation plateau is completed). The analysis was then performed on the final cycle.

The specimen was monitored during the test with a Reflex Nikon D5100 camera, equipped with a Macro lens (AF-S VR Micro-Nikkor 105 mm f/2.8G IF-ED), used to acquire pictures of the painted face of the specimen plate at every 3 s. These images were used to determine the displacement and the strain on the specimen surface by means of 2D DIC [13]. This is a contactless full field experimental technique that allows to estimate the displacement/strain experienced in the flat surface of a component by tracking the speckle movement and distortion. The MATLAB open source 2D DIC program Ncorr [14] was used to cross-correlate the pictures, obtaining displacement and strain maps during the test.

3. Strain and stress calculation

3.1. Standard analysis

For the standard analysis, strains were calculated from the crosshead displacement and stresses as force measured by the load-cell, divided by initial cross-sectional area.

In compliance with the ASTM F2516 – 14 guidance [6] the upper plateau strength σ_{UPS} was measured as the stress at 3% of strain during the loading of the sample, and the lower plateau strength σ_{LPS} as the stress at 2.5% of strain during the unloading of the sample.

The Young's moduli of the austenitic and martensitic phases were calculated by fitting the modulus line to the fully transformed stress–strain curves (i.e. before and after the transformation plateaus) by least-squares regression analyses. As the regions close to the upper and lower plateaus initiation are characterised by significant departures from linearity, the austenitic modulus was calculated on the portion of the loading curve up to a stress σ_E, at ¾ between σ_{LPS} and σ_{UPS}:

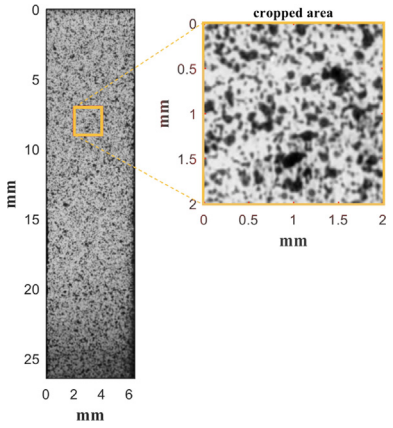

Fig. 1. Specimen speckle surface.

$$\sigma_E = \sigma_{LPS} + \frac{3}{4}(\sigma_{UPS} - \sigma_{LPS}). \quad (1)$$

Similarly, the martensitic modulus was calculated on the portion of the unloading curve from the maximum applied stress to σ_E.

For the determination of the mechanical parameters, the plateau curves were fitted with straight lines, as per standard practice [1516] by least-squares regression analyses. The initial and final transformation stresses between the two crystal phases (namely, the initial stress for the austenite to martensite phase transformation σ_s^{AM}; the final stress for the austenite to martensite phase transformation σ_f^{AM}; the initial stress for the martensite to austenite phase transformation σ_s^{MA}; and the initial stress for the martensite to austenite phase transformation σ_f^{MA}) were obtained from the intersection between these lines and those used to fit the regions where the Young's moduli were estimated. The intersection points at the ends of the upper plateau were used to determine the transformation strain associated with the austenite to martensite transformation ε_L.

3.2. DIC analysis

As previously mentioned, the usual stress and strain calculation described above does not take into consideration the inhomogeneity due to the presence of local regions of different material phases, which nucleate in Lüders bands and progressively expand to occupy the entire gauge length [17]. The strain maps determined applying DIC on Nitinol can overcome this issue, as they are able to clearly identify the regions where the specimen is in the austenitic and martensitic phase, with the latter characterised by much higher strain levels [13]. However, these are not free from the limitations intrinsic in the technique and in the specific experiment. In fact, evaluation of deformation in DIC is based on the assumption of continuity of displacements over the surface, which makes it unsuitable to provide accurate data in regions where there are discontinuities [18]. Moreover, when the analysis is performed in the transformation regions separating the austenitic and martensitic portions, these keep changing between the successive images that are used to perform the correlation. This results in the presence of a thin band (typically of a few tenths of a millimetre) at the interface between the austenitic and martensitic phases, characterised by a gradual variation between the strains identifying the two regions. This appears clear in Fig. 2, where the propagation of the front of phase transition between two successive images is represented together with the regions where the gradual variation is predicted by the technique. Hence, caution must be adopted when analysing the strain data estimated in this transition band, where data are of difficult interpretation. In the proposed approach, two threshold strain values were set at 20% and 80% of ε_L, distinguishing three zones: austenite, martensite and an indeterminate band. The latter was excluded from the computation of the mean values of strain, as shown in Fig. 2.b.

True stresses were calculated as the ratio between the force recorded at the loadcell and the actual cross-sectional area of the analysed region of interest (ROI), estimated as:

$$\sigma = \frac{F}{w \cdot t \left(1 + \bar{\varepsilon}_{xx}\right)^2} \quad (2)$$

where w and t are the width and thickness of the specimen, respectively, and $\bar{\varepsilon}_{xx}$ is the mean strain measured orthogonally to the direction of the load (horizontal direction) for the entire ROI. Here, it is assumed that the lateral strain is the same along the width and along the thickness of the specimen.

The Young's moduli of the austenitic and martensitic configurations were calculated from DIC data as ratio between the true stress and the mean strains over a region of interest covering the whole specimen, with exception of two regions in the grips proximity of length equal to the width of the specimen ($ROI_{E,v}$ in Fig. 3.a). For consistency with the standard analysis, the same portion of the stress–strain curve and the same fitting approach as described above for the moduli calculation were used. For these cases, as the whole specimen is in a single phase (either austenite or martensite), the homogeneity assumption can be considered accurate.

A convenient feature of DIC approaches is that they evaluate the whole plain strain tensor, from which it is straight forward to obtain the Poisson's ratio [19]. The Poisson's ratios of the austenitic and martensitic configurations were calculated from DIC data over the same ROI ($ROI_{E,v}$ in Fig. 3.a) and obtained as negative of the ratio of the mean transverse strain in the region, $\bar{\varepsilon}_{xx}$, to the mean axial strain in the region, $\bar{\varepsilon}_{yy}$.

The phase transformation process is characterised by the propagations of Lüders bands, which typically form at an angle of about 55° from the specimen axis [20], thus determining the simultaneous presence of austenite and martensite along the transverse sections crossing the bands. As these two crystal phases are characterised by significantly different Young's moduli, this can result in the local departure of the neutral axis from the centre of gravity of the specimen and the onset of a bending moment. The presence of bending produces local variations of strains and stresses that increase the uncertainty in the stress–strain parameters determined from standard tests. In order to minimise this effect, the features of DIC can be exploited to focus on small ROIs, so as to reduce the variation in the measured parameters. However, although the reduction in the ROI can provide accurate values of the local strains, the associated local stress is more uncertain, especially if a bending moment is superposed to the tensile load. The maximum eccentricity of the neutral axis will be reached when the transformation occurs with a single front within the sample un-gripped area. In this case, the neutral axis will also coincide with the interface between the two phases, which will be located at a distance from the axis of the cross section equal to:

$$e_{max} = \frac{w}{2} \cdot \frac{1 - \sqrt{2}}{1 + \sqrt{2}} = -0.086w \quad (3)$$

Under these conditions, it can be demonstrated that, assuming an extreme ratio between the Young's moduli of the austenitic and martensitic phases equal to 2, a square ROI region covering 25% of the specimen width and centred at the geometric axis of the specimen would reduce the effect of the spurious bending stress on the

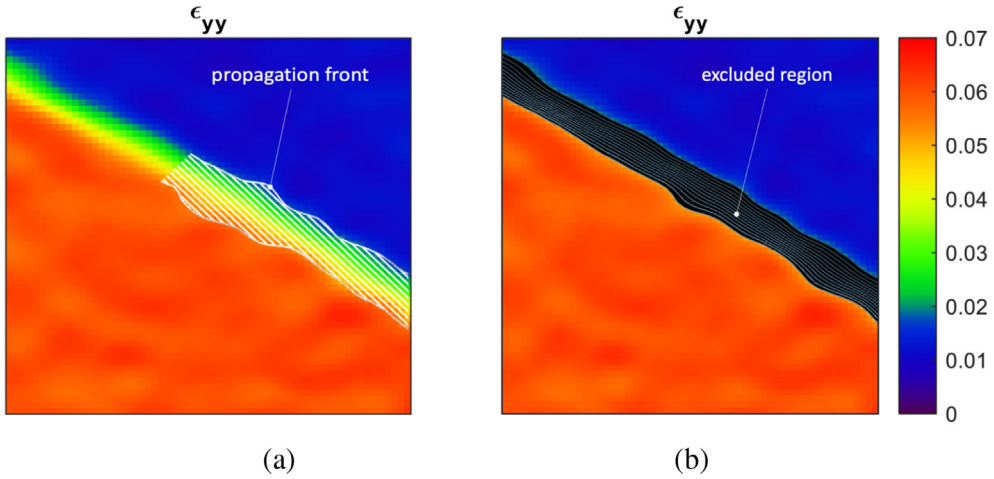

Fig. 2. Propagation of the front of phase transition observed in a generic ROI between two successive images, superposed to the region of gradual strain variation predicted by the DIC technique (a); and strain map after exclusion of the transition region (b).

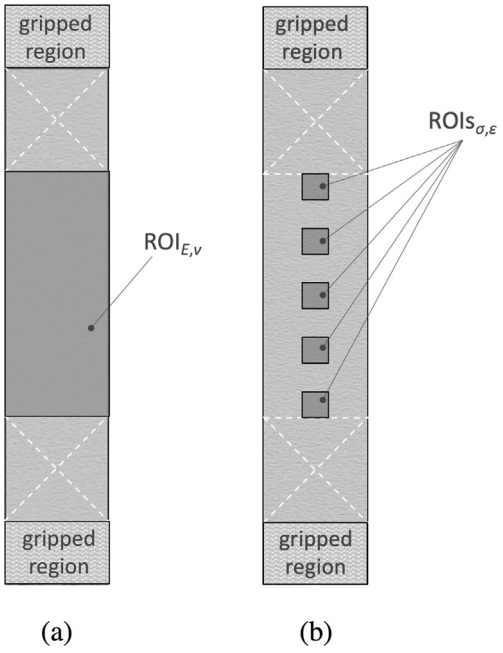

Fig. 3. Regions of interest selected for the calculation of the Young's moduli and Poisson's ratios (a); and for the determination of the stress–strain parameters (b).

average stress calculated through equation (2) of one order of magnitude (see Appendix A, equation (A9)). This selected ROI size allows an accurate strains measurement by focusing on a small region, without compromising the accuracy in the stress determination.

This is in particular true when the maximum bending moment is assumed to keep below:

$$M_{max} \approx \frac{tw^2}{6} \cdot (\sigma_{UPS} - \sigma_{LPS}). \quad (4)$$

In fact, for higher values, the cross sections immediately adjacent to the transformation front where the martensitic transformation has covered the full section would not be able to remain in the martensitic phase and, in the compressed side, would return to austenite.

The maximum expected error in the stress determination would be around 0.12 times the difference between the upper and lower plateau strengths (see Appendix A, equation (A15)). Please notice that the above mentioned behaviour is based on an extreme conservative condition, as the ratio between the austenitic and martensitic Young's moduli is normally lower than 2, and the Lüders bands tend to separate into striae in the regions of high bending moment, thus reducing the eccentricity of the neutral axis, the peak of bending stress and the error in the stress measurement. Moreover, the mentioned bending moment induced by the mismatch in Young's modulus of the two phases is partially counterbalanced by the bending moment produced by the curvature taken by the specimen as effect of the higher elongation experienced by the specimen side with more interested by the martensitic transformation (see also Section 5 for a more in-depth analysis).

Hence, in order to obtain results representative of the whole specimen, the analysis of the stress–strain relationship was performed and averaged over five square regions of interest ($ROIs_{\sigma,\varepsilon}$) of equal size, with square side equal to 25% of the specimen's width and centre located on the vertical axis, evenly spaced along the sample length so as to cover the whole region up to a distance from the grips equal to the specimen width (see in Fig. 3.b).

The initial and final transformation stress between the two crystal phases and the transformation strain ε_L were determined as described above for the standard analysis.

Another interesting additional parameter determined from the DIC analysis was the Poisson's ratio associated with the transformation, ν_T, here defined as the negative of the ratio of the transverse transformation strain ε_{Lx} to the axial transformation strain ε_L calculated over the $ROI_{E,v}$ (see Fig. 3.a).

4. Results

4.1. Standard analysis

Stress-induced martensitic transformation was achieved for the whole gauge length at a peak deformation of 6%, when the upper transformation plateau appeared to have been completed.

The stress–strain curve obtained from the tensile machine output is represented in Fig. 4.a. The curve starts with a smooth and linear behaviour during the austenitic specimen deformation, up to the initiation of the phase transformation (portion *O-A* in Fig. 4.a). This is associated with an initial loss in linearity (portion *A-B* in Fig. 4.a), followed by a sudden drop in the stress at point *B* in Fig. 4.a. Then the stress plateaus up to point *C* in Fig. 4.a, achieving large increases of strains with relatively reduced changes in the

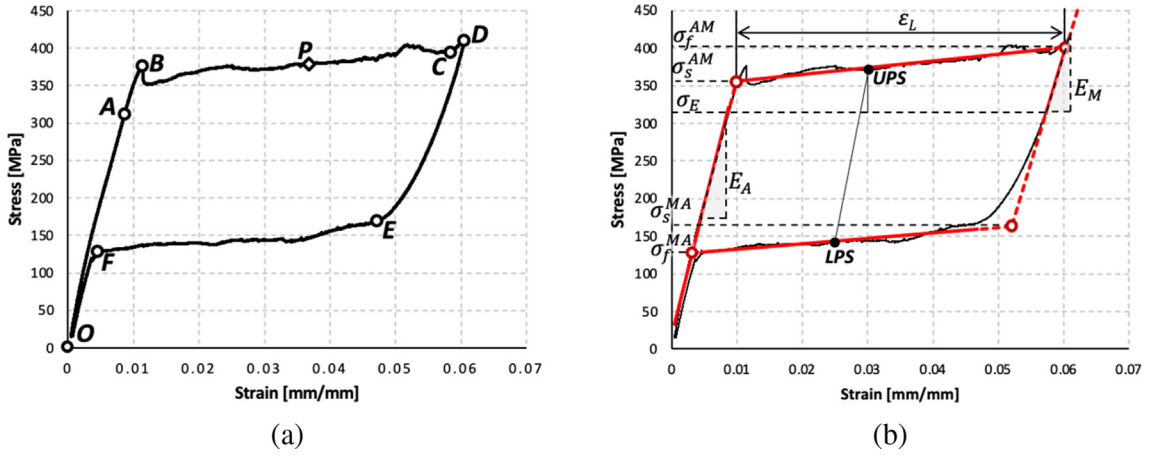

Fig. 4. Stress–strain curve obtained from the tensile machine output (a); and fitting used for the determination of the parameters defining the mechanical behaviour of the material (b).

stress level. Once the entire gauge length of the specimen has transformed, the material swaps to the Young's modulus of the martensitic phase, terminating the plateau region (portion *C-D* in Fig. 4.a). Then the load is gradually removed, recovering pseudo-elastically the entire strain, through the re-transformation into the austenitic phase achieved along the lower plateau (portion *E-F* in Fig. 4.a). This is associated with the nucleation of austenite in unloading Lüders bands, followed by a linear elastic return to the initial unloaded configuration (portion *F-O* in Fig. 4.a).

The σ_{UPS} and σ_{LPS} were respectively equal to 373.3 MPa and 143.6 MPa, giving a value of σ_E equal to 315.87 MPa. The austenitic Young's modulus was equal to 34.7 GPa; and the martensitic Young's modulus, calculated during the unloading from the peak stress of 411.1 MPa to σ_E was 28.8 GPa (17.0% lower than the austenitic one).

The fitted straight lines used for the determination of the parameters defining the mechanical behaviour of the material are displayed in Fig. 4.b. The initial and final stresses defining the upper plateau wereσ_s^{AM} = 356.8 MPa andσ_f^{AM} = 402.4 MPa, respectively; while the initial and final stresses defining the lower plateau wereσ_s^{MA} = 163.7 MPa andσ_f^{MA} = 127.9 MPa, respectively. The transformation strain associated with the austenite to martensite transformation ε_L was equal to 5.1%.

All mechanical characteristics obtained with the standard analysis are summarised in Table 1.

4.2. DIC analysis

The maps of the horizontal (*U*) and vertical (*V*) displacements obtained from Ncorr postprocessing at a generic instant *P* of the upper plateau (as indicated in Fig. 4.a) are represented in Fig. 5.a and b, respectively. These reveal that, for the analysed instant, the deformation is substantially higher at the bottom portion of the specimen. Moreover, the maps of *U* and *V* are not symmetrical about the axis of the specimen, confirming the presence of lateral deflections and local curvatures.

The associated maps of the horizontal and vertical strains ε_{xx} and ε_{yy} are reported in Fig. 5.c and d, respectively. The strain components clearly indicate a bipolar behaviour, with portions of the specimen (the bottom portion for the selected instant) undergoing very high levels of vertical strain (about 7%), associated with substantial lateral contraction (around 3.5%). These appear uniformly distributed up to the Lüders bands. This behaviour is consistent with the crystal rearrangement produced by the transformation into martensite. The level of strains experienced by the region in its austenitic state are negligible, when compared with the bottom region. As mentioned above, a band of gradual passage from the strains characterising the two regions, where strains are considered indeterminate, can be observed in the maps. This, in the presented test, had a thickness of about 0.3 mm, which is consistent with the propagation of the martensitic region between the two instants used for the image correlation.

Table 1
Mechanical characteristics obtained with the different approaches.

Parameter		Standard analysis	DIC reduced ROI	Variation
E_A	[GPa]	34.7	39.0	+ 12.0%
E_M	[GPa]	28.8	30.8	+ 7%
ν_A		–	0.46	
ν_M		–	0.40	
ν_T		–	0.50	
σ_s^{AM}	[MPa]	356.8	378.6 (±1.1%)	+ 6.1%
σ_f^{AM}	[MPa]	402.4	401.9 (±1.4%)	+ 0.1%
σ_{UPS}	[MPA]	373.3	387.2 (±1.3%)	+ 3.7%
σ_s^{MA}	[MPa]	163.7	150.3 (±2.2%)	− 8.2%
σ_f^{MA}	[MPa]	127.9	140.0 (±1.6%)	+ 9.5%
σ_{LPS}	[MPA]	143.6	144.3 (±1.1%)	+ 0.5%
ε_L	[%]	5.1	5.3 (±0.4%)	+3.9%

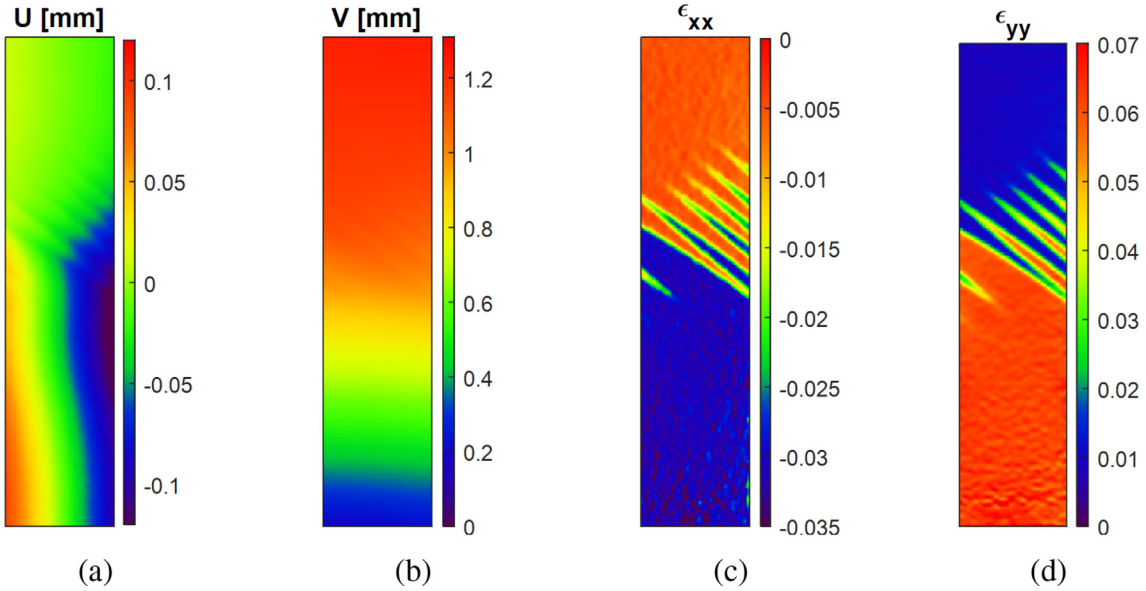

Fig. 5. (a) Horizontal displacement map; (b) vertical displacement map; (c) horizontal strain map; (d) vertical strain map.

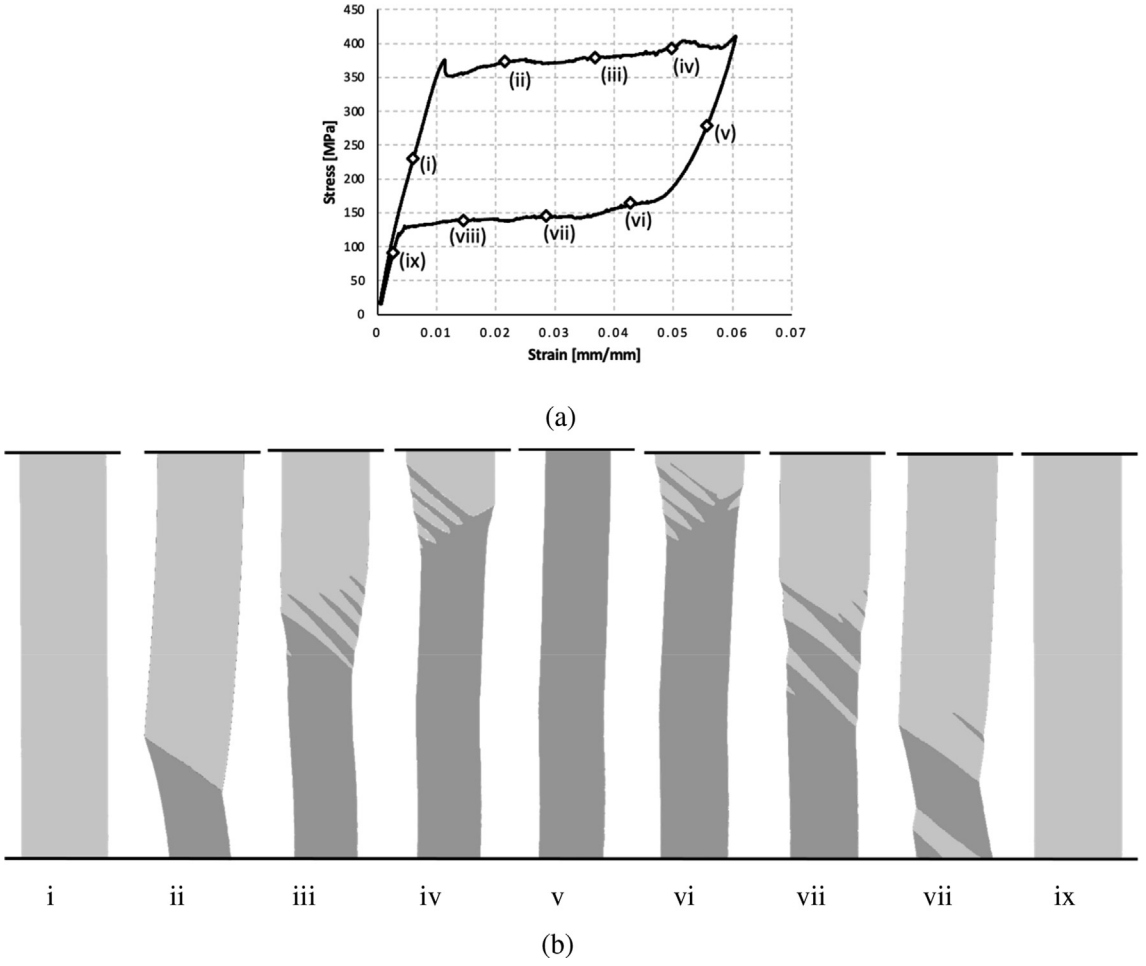

Fig. 6. (a) Instants of the cycle (i-ix) where the sequence of specimen deformations in (b) was determined. Horizontal displacements are amplified of 10 times, and the regions occupied by austenite and martensite, obtained from the strain maps, are represented in light and dark grey, respectively. The complete deformation history is available in the Video 1.

A sequence of deformed shapes of the sample, obtained from the DIC data for the instants i-ix indicated in Fig. 6.a is represented in Fig. 6.b. Horizontal displacements are amplified of 10 times, while the vertical displacements are kept in the same scale as the physical ones. For each instant, the martensitic and austenitic regions obtained from the strains are mapped on the deformed shape (light grey for austenite and dark grey for martensite). The sequence clearly confirms that the transformation from austenite to martensite initiates at one end of the specimen (in proximity of the bottom grip, for the presented test) and then propagates towards the other end, with Lüders bands forming fringes as the front of propagation progresses towards the centre of the specimen. The transformation follows the opposite direction during unloading, maintaining similar features.

The Young's moduli of the austenitic and martensitic configurations calculated from DIC over $ROI_{E,v}$ in Fig. 3.a were equal to 39.0 GPa and 30.8 GPa, respectively. These values are expected to be different from the corresponding constants quantified from the standard approach, because they are based on strains quantified only in a region at a distance from the grips, and on true stresses, estimated on the basis of the transversal strains according to Eq. (2). In particular, both moduli are significantly larger than estimated with the standard analysis (§ 4.1).

The Poisson's ratios for the austenitic and martensitic phases, estimated in the same ROI, were respectively equal to 0.47 and 0.42.

The above results confirm the material inhomogeneity and the presence of spurious bending moments, in support of the hypothesis that the analysis of the stress–strain relationship shall be performed on small regions of the specimen in proximity of the longitudinal axis. The fact that the ratio between the austenitic and martensitic Young's modulus is 1.45, and hence much smaller than the value of 2 previously assumed for the estimation of the stress error, indicates that the accuracy is expected to be higher than the one defined above as acceptable. In addition, the eccentricity of the neutral axis due to the mismatch in Young's modulus of the two phases, measured along the entire specimen's axis as:

$$e_{NA} = \frac{\sum xE(x)}{\sum E(x)}; \tag{5}$$

is only about one quarter of that estimated from Eq. (3).

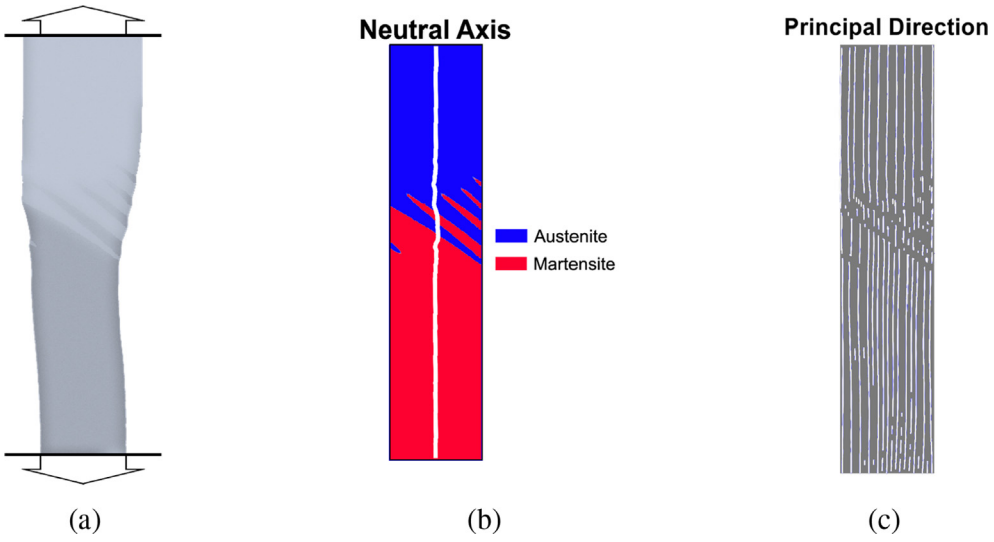

Fig. 7. (a) Shape of the specimen with amplified lateral displacements; (b) map of the specimen showing the austenitic and martensitic regions, and the position of the neutral axis represented by a white line (calculated using Eq. (5)); (c) principal directions determined on the measured strains. All pictures are in relation to the instant P, as indicated in Fig. 4.a.

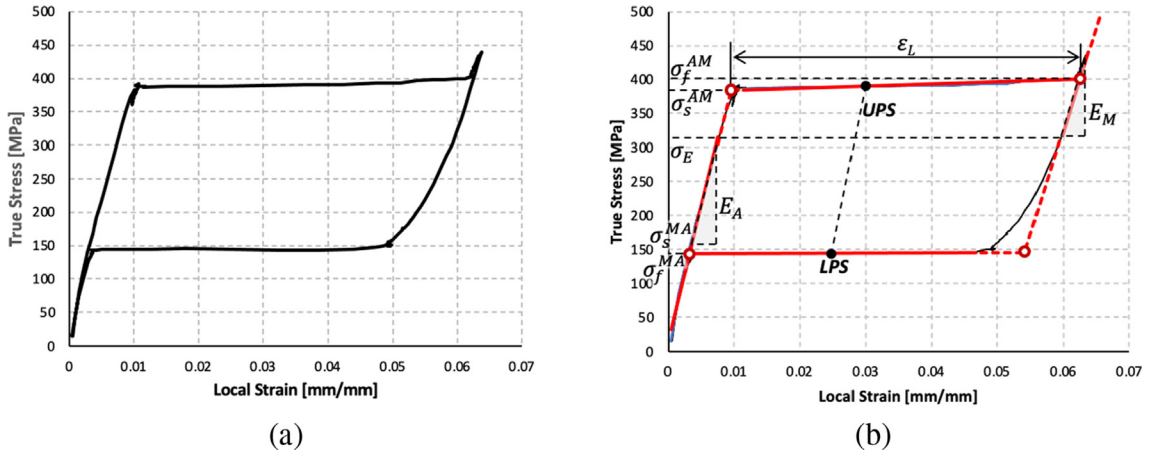

Fig. 8. Typical stress–strain map determined on square ROIs with side equal to 25% of the specimen width (in Fig. 3.b), positioned on the axis of the specimen (a); and fitting used for the determination of the parameters defining the mechanical behaviour of the material (b).

Another useful result is the fact that the maximum principal direction determined from the strain maps is maintained about aligned with the direction of the applied force (±5°) (see Fig. 7). All these considerations confirm that the usual stress calculation over the ROIs$_{\sigma,\varepsilon}$ (the ratio between the force measured at the load-cell divided by the actual cross section for the ROIs$_{\sigma,\varepsilon}$ represented in Fig. 3.b) is an acceptable approximation.

The typical stress–strain diagram obtained from the ROIs$_{\sigma,\varepsilon}$ in Fig. 3.b is represented in Fig. 8 (in particular, the central ROI is used in the figure). The diagrams from the different ROIs are very similar and with very low variability, as indicated by the small standard deviation in the parameters reported below.

The initial and final stresses defining the upper plateau, recomputed using DIC, were respectively σ_s^{AM} = 378.6 (±1.1%) MPa andσ_f^{AM} = 401.9 (±1.4%) MPa; the initial and final stresses defining the lower plateau were respectively σ_s^{MA} = 150.3 (±2.2%) MPa and σ_f^{MA} = 140.0 (±1.6%) MPa; and the upper and lower plateau strengths were σ_{UPS} = 387.2 (±1.3%) MPa and σ_{LPS} = 144.3 (±1.1%) MPa, respectively. Hence, despite maintaining the plateau strength nearly unchanged compared to the standard analysis, significant increase in σ_s^{AM} and σ_s^{MA} and decrease in σ_f^{AM} and σ_f^{MA} indicate a substantial flattening of the two plateaus (more evident for the lower plateau).

The transformation strain associated with the austenite to martensite transformation ε_L estimated with DIC was ε_L = 0.053, and the associated transversal (horizontal) transformation strain was ε_{Lx} = -0.027, indicating a Poisson's ratio ν_T associated with the transformation equal to 0.5.

The stress–strain curve obtained from this approach (e.g. curves displayed in Fig. 8a,b) are much closer to the idealised set of straight lines that are fitted to extract the parameters defining the mechanical response of Nitinol. Therefore, they are particularly suitable to characterise the material in a more accurate and consistent way.

The parameters obtained from this approach are summarised in the second data column in Table 1, aside the mechanical characteristics obtained with the standard analysis.

5. Discussion

In the common practice and in compliance with the available regulatory standards, the stress and strain in Nitinol specimens subjected to uniaxial tension testing are assumed uniformly distributed over a finite area comprised in the extensometer gauge length. However, the present study confirms that this assumption cannot be considered valid. The strain distribution (shown in Fig. 5.c,d and used to obtain the maps of phase distribution in the sequence in Fig. 6) suggests that the material instantaneously switches between the austenitic and martensitic configurations when the plateau stress is locally reached. This bimodal behaviour has major consequences. In fact, in order to maintain geometrical congruence, the interface between the region where the martensitic transformation has occurred, which experiences significant levels of longitudinal and lateral deformation, and the portion of the specimen which is in the austenitic phase needs to take a specific angle with respect to the axis. With reference to Fig. 9.a, as an effect of the transformation strain ε_L experienced by the martensitic region, it will be:

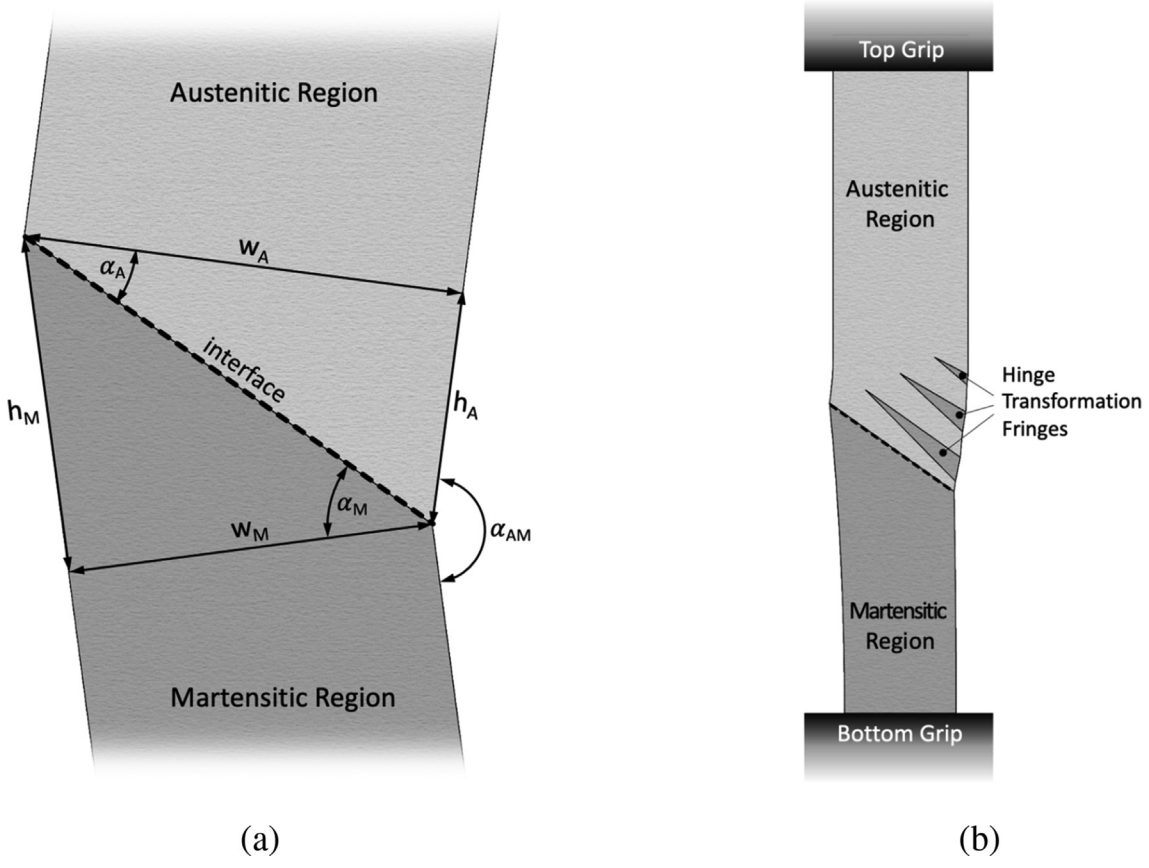

Fig. 9. Schematic representation of the region of interface between the austenitic and martensitic regions (a), and of the full specimen in the transformation plateau region (b).

$$h_M = h_A(1 + \varepsilon_L) \tag{6}$$

and

$$w_M = w_A(1 - \nu_T \varepsilon_L) \tag{7}$$

where ν_T corresponds to the Poisson's ration associated with the phase transformation. Basic geometrical considerations (reported in Appendix B) lead to the determination of the angles that need to establish between the interface (transformation front line) and the transversal section of the austenitic and martensitic regions, α_A and α_M, respectively:

$$\alpha_A = \arctan \sqrt{\frac{2\nu_T - \nu_T^2 \varepsilon_L}{2 + \varepsilon_L}}; \tag{8}$$

and

$$\alpha_M = \arcsin\left[(1 + \varepsilon_L)\sin \alpha_A\right] \tag{9}$$

Interestingly, these angles do not depend on the mechanical properties of two phases, but only on the transformation strain and on the transformation Poisson's ratio. As in our case $\varepsilon_L = 0.053$ and ν_T = 0.5, the equation above provides an angle of 34.73° for α_A and 36.86° for α_M, with an average inclination of the transformation front with respect to the cross section of the specimen of $\alpha = 35.80^{\circ}$. Moreover, because of the same phenomenon, the axes of the austenitic and martensitic regions will tend to be angled with respect to each other, aiming at a misalignment given by $\alpha_M - \alpha_A$, which in the presented case is of 2.13°. As a result, the specimen splays towards the side where the martensitic length is greater, as shown in Fig. 6.b(ii). This is necessarily associated with the introduction of a spurious bending moment. Moreover, the presence of a fixed constrain at the grips requires that the length of the specimen in the left and right sides stays approximately equal and the axes at the top and bottom maintain their alignment during the test. Hence, as the front of transformation progresses towards the midspan, the bending moment increases until, eventually, a set of new fringes form, serving as hinge regions which allow the specimen to realign its axes at the top and bottom ends and relax the bending moment, as schematically shown in Fig. 9.b (this is evident in the experimentally determined sequence reported in Fig. 6.b, starting from instant iii). These fringes allow to balance the percentage of austenite (whose stretching is negligible) and martensite (which is highly stretched) in the left and right sides of the specimen, so as to match the vertical length of the specimen for the different vertical lines. This phenomenon produces new transformation fringes at the side of the specimen where the length of the stretched martensitic region is inferior and, therefore, needs to be increased. The described process justifies and explains the formation of the Lüders bands which, consistently with the literature [7,8], were observed in the presented study at an angle of about 35° from the cross-sectional plane (corresponding to about 55° from the specimen's longitudinal axis). It is reasonable to expect that similar phenomena may occur along the thickness, although with much smaller influence on the overall specimen behaviour, due to reduced dimension.

The implication of the described phenomenon is that the same cross section may be characterised by multiple regions with alternative crystal configurations and, therefore, different mechanical properties. This, as described above, results in departures of the neutral axis from the cross-sectional centre of gravity, that contribute to locally introduce an additional bending moment. However, as the neutral axis tends to move towards the side where the Young's modulus is greater (the austenitic region), this effect does not cumulate with the one described above, but is does locally counterbalance it.

The phenomena described above refute the very basis of uniaxial tension tests, questioning the suitability of current practices to derive information on the material behaviour which should be compatible with the high-risk applications that rely on Nitinol. In fact, the stress–strain curve obtained from the tensile machine output, as shown in Fig. 3, represents an average in time of a combination of effects which interest different and varying regions of the specimen. This is reflected in the irregularity of the plateaus, that makes particularly difficult to identify objective criterial to idealise the diagram and extract the common material characteristics.

In this test, the testing machine crosshead was used to determine the strain (this is accepted by the ASTM standards [5,6]), but similar issues are to be expected with the use of mechanical extensometers. In fact, any practical distance between the extensometers knife edges would still be associated with highly inhomogeneous behaviours. Moreover, the propagation of the transformation front and hinge fringes at a large angle with the specimen's cross section (larger than 35°) would introduce errors and further complexity in the interpretation of the results.

Most importantly, all phenomena described above that can affect the results are essentially dependent on the specimen dimensions and testing setup, making the measurement of the mechanical characteristics of the material very difficult to generalise. This indicates a clear need for a new approach allowing a more objective analysis, especially in consideration of the high-risk healthcare applications where Nitinol is commonly used, that require the highest levels of optimisation. In this scenario, features of full-field and non-contact measurement such as those of DIC techniques become essential to provide a proper investigation of the material behaviour.

The stress–strain curve obtained from the DIC results (in Fig. 8) on smaller ROIs (25% of the specimen's width in the presented study) focalised along the geometric axis of the specimen, so as to minimise bending stresses, become very repeatable and more suitable to characterise the material behaviour. Comparing the stress–strain diagrams obtained with the standard and DIC approaches (see Fig. 10), it is evident that the sudden drop in the stress observed in the data from the tensile machine output is an artefact due to the phenomena described above. Instead, at local level, the reduction in load associated with the triggering of the martensitic transformation at a different region of the specimen, is perceived as a small unloading along the austenitic curve, then compensated by further increase in stress, until transformation initiates in the analysed ROI (Video 2 reports Stress–strain map history determined with the standard and DIC approaches). As a result, the plateau flattens substantially at levels of stress closer to the final plateau stress. Flattening of the plateau is even more evident for the lower plateau, where the difference between the start and finish transformation stress is in the order of 7%.

Another interesting correction introduced by the local DIC analysis is in the slope of the martensitic phase, which contrary to the standard approach appears to be well overlapping for the loading and unloading branches.

As expected, true stresses determined from the DIC analysis are substantially larger than the engineering stresses, resulting in significant increase in the transformation stresses and in the Young's moduli of the two materials than predicted with the standard approach.

These differences are due to the high Poisson's ratios observed for the austenitic and martensitic phases ($\nu_A = 0.46$ and $\nu_M = 0.40$), which appear to be much larger than the value of 0.33 commonly assumed in the literature for both phases [21] and produce substantial contractions in the actual cross section. This interesting finding compares well with measurements of the Poisson's ration performed on polycrystalline martensitic NiTi with

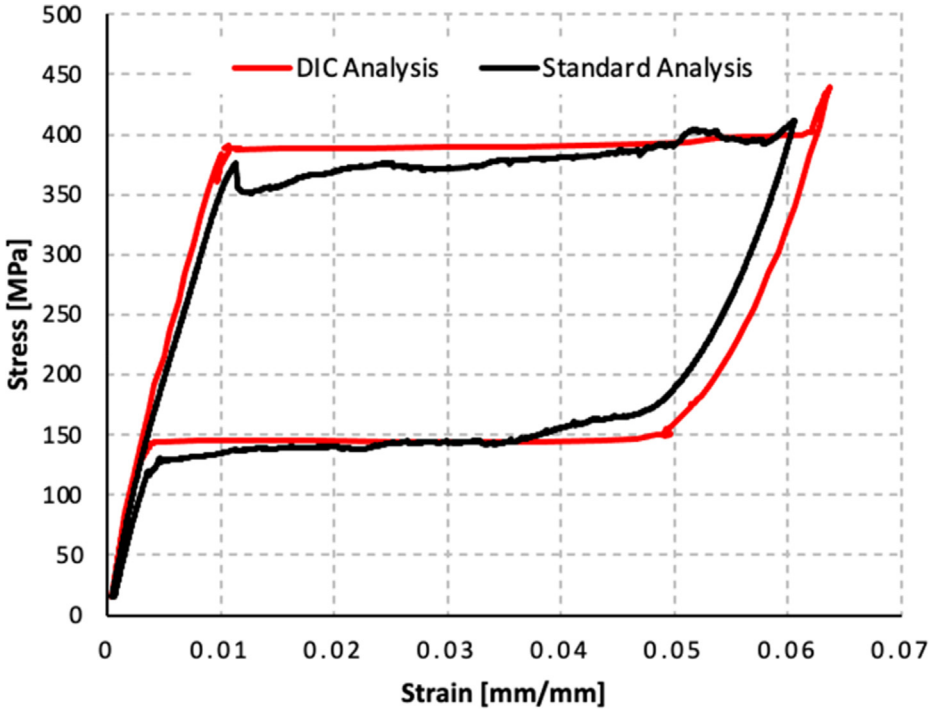

Fig. 10. Stress–strain map determined with the standard and DIC approaches described in the article.

neutron diffraction, which indicated a value of v_M equal 0.39 ± 0.03 [22]. Similarly, the material data provided in a computational study from Kleinstreuer *et al.* [23] indicate a value of 0.46 for both v_A and v_M. For what concerns the Poisson's ratio associated with the transformation v_T, this appears more consistent with the data in the literature, that typically refer to a value of 0.5 [17]. As the Poisson's ratios are critical for a correct description and modelling of the material's behaviour, these contrasting data clearly indicates a gap in the current literature.

Although the presented approach may contribute to determine more objective and representative parameters of the mechanical properties, less dependent of the specific test setup and conditions, this still needs to be accompanied by the implementation of more advanced constitutive models for NiTi alloys, able to better replicate the inhomogeneous phenomena observed in the test.

6. Conclusions

This work analyses the main sources of error affecting the reliability of standard uniaxial tension tests for the mechanical characterisation of superelastic Nitinol aloys. In particular, the stress induced transformation that provides the super-elastic behaviour also causes the presence of regional inhomogeneities in the test specimen, associated with the formation of Lüders bands, lateral displacements and spurious bending moments superposed to the tensile load. These phenomena limit the reliability of standard characterisation methods to provide parameters sufficiently accurate to achieve an adequate description of the material and to exploit its features optimally. DIC analysis, by allowing a full field detection of the strains, can help not just to clarify, but also to overcome these limitations. In fact, performing the mechanical characterisation in regions of interest sufficiently small, in proximity of the specimen's axis, allows to minimise the spurious effects and determine more accurate and consistent parameters, that describe a material response which appear to be closer to the ideal one and independent of the testing setup. This is characterised by flatter plateaus that closely match straight lines suitable to extract parameters defining the mechanical response of Nitinol. Therefore, they are particularly suitable to provide a more accurate and consistent characterisation of the material. Still, results are affected by assumptions and approximations in the determination of the stress and in the exclusion of the regions at the interface between the two crystal phases. Nevertheless, the proposed approach surely provides a substantially improved characterisation of the material, much needed to support the selection of specific alloys and thermomechanical treatments, and to achieve optimised levels of safety and efficacy in the most critical applications where Nitinol is employed.

Declaration of Competing Interest

The authors declare that they have no known competing financial interests or personal relationships that could have appeared to influence the work reported in this paper.

Acknowledgements

Authors wish to acknowledge Dr Alessandra Monteleone, Dr Danila Vella, Dr Alessia Viola e Mr Giulio Musotto for their advice, suggestions and helpful discussions.

This work was supported by the Programma Patto per il Sud Regione Sicilia - FSC 2014/2020 239 (Project Computational Molecular Design and Screening CHeMISt) and by the British Heart Foundation 240 (FS/16/6/31821).

Data availability

The raw data required to reproduce these findings are available to download from:https://data.mendeley.com/datasets/jyg9fywx3w/1

Appendix A

Selection of the $ROIs_{\sigma}$ dimension based on the maximum estimated error on the stress determination.

In order to maintain geometrical congruence, the interface between the region where the martensitic transformation has occurred and the portion of the specimen which is in the austenitic phase needs to take a specific angle with respect to the axis. Therefore, the cross sections hosting the front of transformation are partitioned into multiple regions with different mechanical properties. This results in departures of the neutral axis from the cross-sectional centre of gravity, contributing to locally introduce a bending moment.

Based on the common theory of composite beams, for each cross-section, the eccentricity of the neutral axis will depend on the cross-section geometry, on the distribution of the regions with different Young's modulus and, in the case where only two Young's moduli are present, on their ratio n. In particular, the maximum eccentricity of the neutral axis will be reached when the transformation occurs with a single front.

In fact, if the front of the martensitic phase reaches a distance m from the origin of a reference system positioned at the left end of the specimen cross-section, with the x-axis aligned with the specimen width w (see Fig. A1.a), the position of the neutral axis can be determined as:

$$x_{NA} = \frac{A_M x_M + nA_A x_A}{A_M + nA_A} = \frac{1}{2} \cdot \frac{m^2 + n(w^2 - m^2)}{m + n(w - m)} \tag{A1}$$

and the eccentricity of the neural axis is:

$$e_{NA} = x_{NA} - \frac{w}{2} = \frac{1}{2} \cdot \frac{m^2(1-n) - mw(1-n)}{nw + m(1-n)}. \tag{A2}$$

This eccentricity will be maximum when:

$$\frac{de_{NA}}{dm} = (n-1)\frac{(n-1)m^2 - 2nwm + nw^2}{[(n-1)m - nw]^2} = 0; \tag{A3}$$

which has acceptable solution:

$$m = w\frac{\sqrt{n}}{1+\sqrt{n}}. \tag{A4}$$

Substituting into the expression of the eccentricity:

$$e_{NAmax} = \frac{w}{2} \cdot \frac{\sqrt{n}-1}{\sqrt{n}+1}. \tag{A5}$$

In this case, the position of the neutral axis in the reference system, x_e and that of the front of transformation, m, are coincident. In fact:

$$x_e = \frac{w}{2} + e_{NAmax} = \frac{w}{2}\left(1 + \frac{\sqrt{n}-1}{\sqrt{n}+1}\right) = w\frac{\sqrt{n}}{1+\sqrt{n}} = m. \tag{A6}$$

Hence, the stress associated with the resulting bending moment M (excluding the stress produced by the normal load) will have the distribution represented in Fig. A1.b, with:

$$\sigma_{Mmax} = \frac{m}{n(w-m)}\sigma_{Amax} \tag{A7}$$

The mean stress calculated over a centred specimen length of dimension $p \cdot w$, is given by:

$$\begin{aligned}\bar{\sigma}_x &= \frac{\frac{1}{2}\left(m - \frac{1-p}{2}w\right)^2 \frac{\sigma_{Mmax}}{m} - \frac{1}{2}\left(w - m - \frac{1-p}{2}w\right)^2 \frac{\sigma_{Amax}}{w-m}}{p \cdot w} \\ &= \left[\left(\frac{\sqrt{n}-1}{1+\sqrt{n}} + p\right)^2 - n\left(\frac{1-\sqrt{n}}{1+\sqrt{n}} + p\right)^2\right]\frac{(1+\sqrt{n})}{8np}\sigma_{Amax}\end{aligned} \tag{A8}$$

Assuming a reasonably conservative value of $n = E_A/E_M = 2$, analysing a region equal to 25°% of the specimen width ($p = 0.25$):

$$\bar{\sigma}_x \approx 0.10\sigma_{Amax} \tag{A9}$$

Determination of the maximum expected error in the stress determination, in relation to the upper and lower plateau strength.

The maximum stress in the austenitic region is given by:

$$\sigma_{\max A} = \frac{nM}{I}(w-m) = \frac{nwM}{I}\left(1 - \frac{\sqrt{n}}{1+\sqrt{n}}\right) = \frac{wM}{I} \cdot \frac{n}{1+\sqrt{n}} \tag{A10}$$

where I is the moment of inertia of the cross-section, and M is the value of the bending moment at the considered cross-section.

The moment of inertia for a composite beam can be calculated applying the parallel axis theorem, as:

$$\begin{aligned}I &= \left[\frac{tm^3}{12} + \frac{tm^3}{4}\right] + n\left[\frac{t(w-m)^3}{12} + \frac{t(w-m)^3}{4}\right] \\ &= \frac{tm^3}{3} + n\frac{t(w-m)^3}{3} = \frac{tw^3}{3} \cdot \frac{n}{(1+\sqrt{n})^2}\end{aligned} \tag{A11}$$

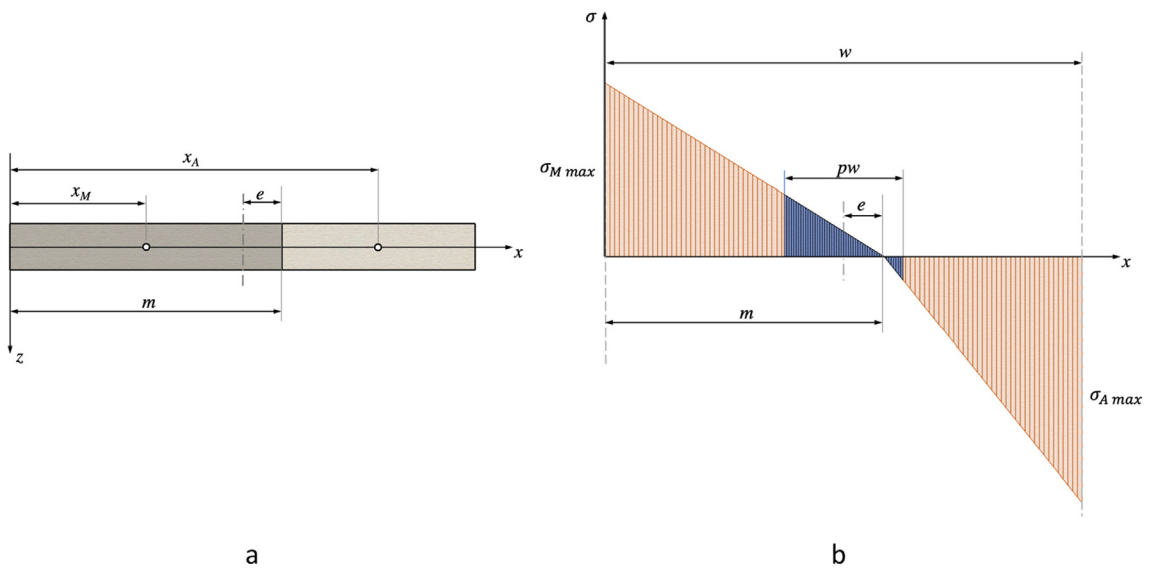

Fig. A1. (a) Specimen cross-section; (b) Bending moment diagram.

Hence:

$$\sigma_{\max A} = \frac{wM}{I} \cdot \frac{n}{1+\sqrt{n}} = \frac{3M}{tw^2}(1+\sqrt{n}) \tag{A12}$$

For the condition in Eq. (4), the expression for the maximum stress in the austenitic region becomes:

$$\sigma_{\max A} = \frac{1+\sqrt{n}}{2}(\sigma_{UPS} - \sigma_{LPS}) \tag{A13}$$

For the conservative assumption that $n = 2$, this value becomes:

$$\sigma_{\max A} = \frac{1+\sqrt{2}}{2}(\sigma_{UPS} - \sigma_{LPS}) \approx 1.2(\sigma_{UPS} - \sigma_{LPS}) \tag{A14}$$

Based on Eq. (A9), the error introduced by the spurious bending stress on the average stress calculated through Eq. (1) is one order of magnitude lower than this value, hence:

$$\bar{\sigma}_x \approx 0.12(\sigma_{UPS} - \sigma_{LPS}) \tag{A15}$$

Appendix B

Angles between the regions at the interface between the two phases

Due to the large transformation strain ε_L and transformation Poisson's ratio v_T, the martensitic region of the specimen is characterised by significant dimensional changes compared to the untransformed austenitic region. Hence, in order to preserve continuity, the interface between two phases and the two regions at the interface will needs to take specific angles that, in first approximation, can be determined from basic geometric considerations.

Assuming, for simplicity, that the transformation propagates with a single front (see Fig. 9.a), the dimensions of the martensitic triangular region covering the specimen length interested by front will be:

$$h_M = h_A(1+\varepsilon_L); \tag{B1}$$

and

$$w_M = w_A(1 - v_T\varepsilon_L) \tag{B2}$$

Indicating with α_A and α_M the angles between the transformation front line and the transversal section of the austenitic and martensitic regions, respectively, it will also be:

$$h_A = w_A \tan\alpha_A \tag{B3}$$

The Pythagorean theorem can provide the following additional relation, which allows to solve the system:

$$h_A^2 + w_A^2 = h_M^2 + w_M^2 \tag{B4}$$

Combining equations (B1) with (B2), α_A can be determined as:

$$\alpha_A = \arctan\sqrt{\frac{2v_T - v_T^2\varepsilon_L}{2+\varepsilon_L}} \tag{B5}$$

α_M can be determined from the equations below, thanks to the trigonometric relationship:

$$\frac{h_A}{\sin\alpha_A} = \frac{h_M}{\sin\alpha_M}. \tag{B6}$$

In fact, combining equations (B6) with (B3), α_M can be obtained as:

$$\alpha_M = \arcsin[(1+\varepsilon_L)\sin\alpha_A] \tag{B7}$$

- Video 1. Stress–strain map video

Stress–strain map history determined with the standard approaches (in black) and with the DIC approaches calculated for the $ROI_{E,\nu}$ and the central $ROI_{\sigma,\varepsilon}$ (in Fig. 3) represented in green and magenta, respectively.

- Video 2. Amplified specimen deformation video

Video of the amplified specimen deformations of Fig. 6. Where the horizontal displacements are amplified of 10 times, and the regions occupied by austenite and martensite, obtained from the strain maps, are represented in light and dark grey, respectively.

Appendix C. Supplementary data

Supplementary data to this article can be found online at https://doi.org/10.1016/j.matdes.2022.110538.

References

[1] J.P. Oliveira, R.M. Miranda, N. Schell, F.M. Braz Fernandes, High strain and long duration cycling behavior of laser welded NiTi sheets, Int. J. Fatigue 83 (2016) 195–200, https://doi.org/10.1016/j.ijfatigue.2015.10.013.

[2] J.P. Oliveira, D. Barbosa, F.M.B. Fernandes, R.M. Miranda, Tungsten inert gas (TIG) welding of Ni-rich NiTi plates: functional behavior, Smart Mater. Struct. 25 (3) (2016) 03LT01, https://doi.org/10.1088/0964-1726/25/3/03LT01.

[3] W.C. Ke, J.P. Oliveira, B.Q. Cong, S.S. Ao, Z.W. Qi, B. Peng, Z. Zeng, Multi-layer deposition mechanism in ultra high-frequency pulsed wire arc additive manufacturing (WAAM) of NiTi shape memory alloys, Addit. Manuf. 50 (2022) 102513, https://doi.org/10.1016/j.addma.2021.102513.

[4] A. Wadood, Brief Overview on Nitinol as Biomaterial, Adv. Mater. Sci. Eng. 2016 (2016) 1–9.

[5] American Society for Testing and Materials, "ASTM E8/E8M standard test methods for tension testing of metallic materials 1," *Annual Book of ASTM Standards 4*, no. C, pp. 1–27, 2010, doi: 10.1520/E0008.

[6] American Society for Testing and Materials, "ASTM F2516−14: Standard Test Method for Tension Testing of Nickel-Titanium Superelastic Materials," *ASTM International*, p. 6, 2015, doi: 10.1520/F2516-14.2

[7] M. Frost, P. Sedlák, P. Sedmák, L. Heller, P. Šittner, SMA Constitutive Modeling Backed Up by 3D-XRD Experiments: Transformation Front in Stretched NiTi Wire, Shape Memory and Superelasticity 4 (4) (2018) 411–416, https://doi.org/10.1007/s40830-018-0192-x.

[8] L. Zheng, Y. He, Z. Moumni, Effects of Lüders-like bands on NiTi fatigue behaviors, Int. J. Solids Struct. 83 (2016) 28–44, https://doi.org/10.1016/j.ijsolstr.2015.12.021.

[9] D.C. Lagoudas, Shape Memory Alloys: modeling and engineering applications. (2008), https://doi.org/10.1007/978-0-387-47685-8.

[10] J.P. Oliveira, Z. Zeng, S. Berveiller, D. Bouscaud, F.M. Braz Fernandes, R.M. Miranda, N. Zhou, Laser welding of Cu-Al-Be shape memory alloys: Microstructure and mechanical properties, Mater. Des. 148 (2018) 145–152, https://doi.org/10.1016/j.matdes.2018.03.066.

[11] Y. Tanaka, Y. Himuro, R. Kainuma, Y. Sutou, T. Omori, K. Ishida, Ferrous Polycrystalline Shape-Memory Alloy Showing Huge Superelasticity, Science 327 (5972) (2010) 1488–1490.

[12] S. di Leonardo, R. Cappello, G. Burriesci, G. Pitarresi, Investigation of the Thermomechanical Response of Cyclically Loaded NiTi Alloys by Means of Temperature Frequency Domain Analyses, Materials 14 (24) (Dec. 2021) 7866, https://doi.org/10.3390/ma14247866.

[13] M. A. Sutton, J. J. Orteu, and H. W. Schreier, *Image Correlation for Shape, Motion and Deformation Measurements*. Boston, MA: Springer US, 2009. doi: 10.1007/978-0-387-78747-3

[14] J. Blaber, B. Adair, A. Antoniou, Ncorr: Open-Source 2D Digital Image Correlation Matlab Software, Exp. Mech. 55 (6) (2015) 1105–1122, https://doi.org/10.1007/s11340-015-0009-1.

[15] E. McCummiskey, W.M. Dempster, D.H. Nash, T.R. Ashton, D.G. Stevenson, The determination and evaluation of nitinol constitutive models for finite element analysis, Appl. Mech. Mater. 7–8 (2007) 81–88, https://doi.org/10.4028/www.scientific.net/AMM.7-8.81.

[16] E. Masoumi Khalil Abad, D. Pasini, R. Cecere, Shape optimization of stress concentration-free lattice for self-expandable Nitinol stent-grafts, J. Biomech. 45 (6) (2012) 1028–1035.

[17] C. Bewerse, K.R. Gall, G.J. Mcfarland, P. Zhu, L.C. Brinson, A Local and global strains and strain ratios in shape memory alloys using digital image correlation, Mater. Sci. Eng., A 568 (2013) 134–142, https://doi.org/10.1016/j.msea.2013.01.030.

[18] G.M. Hassan, Digital Image Correlation for discontinuous displacement measurement using subset segmentation, Opt. Lasers Eng. 115 (2019) 208–216, https://doi.org/10.1016/j.optlaseng.2018.12.003.

[19] R.H. Pritchard, P. Lava, D. Debruyne, E.M. Terentjev, Precise determination of the Poisson ratio in soft materials with 2D digital image correlation, Soft Matter 9 (26) (2013) 6037–6045, https://doi.org/10.1039/C3SM50901J.
[20] G. Ananthakrishna, Current theoretical approaches to collective behavior of dislocations, Phys. Rep. 440 (4) (2007) 113–259, https://doi.org/10.1016/j.physrep.2006.10.003.
[21] W.B. Cross, A.H. Kariotis, F.J. Stimler, Nitinol characterization study, NASA CR-(1433, 1969.).
[22] S. Qiu, B. Clausen, S.A. Padula, R.D. Noebe, R. Vaidyanathan, On elastic moduli and elastic anisotropy in polycrystalline martensitic NiTi, Acta Mater. 59 (13) (2011) 5055–5066, https://doi.org/10.1016/j.actamat.2011.04.018.
[23] C. Kleinstreuer, Z. Li, C.A. Basciano, S. Seelecke, M.A. Farber, Computational mechanics of Nitinol stent grafts, J. Biomech. 41 (11) (2008) 2370–2378, https://doi.org/10.1016/j.jbiomech.2008.05.032.